APPLIED PHYSICS

Quantum effects in the interaction of low-energy electrons with light

Adamantios P. Synanidis[1], P. A. D. Gonçalves[1], Claus Ropers[2,3], F. Javier García de Abajo[1,4]*

The interaction between free electrons and optical fields constitutes a unique platform to investigate ultrafast processes in matter and explore fundamental quantum phenomena. Specifically, optically modulated electrons in ultrafast electron microscopy act as noninvasive probes that push space–time–energy resolution to the picometer–attosecond–microelectronvolt range. Electron energies well above the involved photon energies are commonly used, rendering a low electron–light coupling and, thus, only providing limited access to the wealth of quantum nonlinear phenomena underlying the dynamical response of nanostructures. Here, we theoretically investigate electron–light interactions between photons and electrons of comparable energies, revealing quantum and recoil effects that include a nonvanishing coupling of surface-scattered electrons to light plane waves, inelastic electron backscattering from confined optical fields, and strong electron–light coupling under grazing electron diffraction by an illuminated crystal surface. Our exploration of electron–light–matter interactions holds potential for applications in ultrafast electron microscopy.

INTRODUCTION

The synergetic relation between short light pulses and free electron beams (e-beams) underlies several recent advances in ultrafast electron microscopy toward a combined subnanometer–subfemtosecond–submillielectronvolt spatiotemporal and spectral resolution, rapidly progressing toward the goal of mapping atomic-scale spatial features and their evolution over unprecedentedly small timescales (*1–8*). A prominent example is photon-induced near-field electron microscopy (PINEM) (*1, 9, 10*), which is based on the synchronous arrival of laser and electron femtosecond pulses at a sampled nanostructure, thus enabling optical-pump/electron-probe spectroscopy to be performed with a nanoscale spatial resolution inherited from the use of state-of-the-art electron optics setups. This approach has been applied to image optical near fields in nanophotonics (*11–14*), the subcycle evolution of those fields (*15–17*), and the nanoscale-resolved fluctuations of the light with which the electron has interacted (*18–20*). PINEM can be regarded as a specific application of the more general concept of stimulated inelastic electron–light scattering (SIELS). The latter has been leveraged to gain control over the free-electron wave function by customizing its interaction with light, including the generation of trains of attosecond electron pulses (*3, 21–23*) and the shaping of the transverse e-beam profile (*24–28*). Laser-assisted photoemission (*29, 30*) constitutes another example of SIELS that can be used to probe the ultrafast dynamics of condensed-matter systems (*31*) and produces interesting effects in the strong-field limit (*32, 33*).

Many of these advances have been accomplished in transmission electron microscopes operating with relatively high e-beam energies ($\gtrsim 30$ keV), orders of magnitude larger than those of the used photons (typically in the electronvolt range) and, consequently, rendering the probability that a single electron interacts with a single photon (e.g., one quantum of a confined optical mode) much smaller than unity. Such a weak electron–light interaction limits applications in metrology, imaging of atomic-scale excitations, and the study of nonlinear phenomena. For robust structures, the problem is circumvented in SIELS by using intense laser pulses (*11–13*), but this approach cannot be extended to sensitive specimens such as biological materials. Phase matching between the electron excitation and the light field can also boost the interaction (*34–38*), although this strategy is only practical in specialized structures that host modes with evanescent optical fields in vacuum.

Unexpectedly, in the linear electron–photon interaction regime, describing electrons as classical point-like charges produces the same results as a quantum-mechanical treatment in which electron recoil is ignored (*6*). Notice, however, that recoil has been theoretically (*39, 40*) (on kinematic grounds) and experimentally (*40*) (at kiloelectronvolt emission energy) shown to produce discernible effects in the energy–angle distribution of Smith–Purcell radiation emission produced by electron interaction with a grating. Likewise, the wave function of energetic electrons in PINEM, and more generally in SIELS, is modified by a global factor that encapsulates the interaction with light through a single complex parameter that depends linearly on the optical field (*3, 6, 9, 10, 41, 42*) and is therefore unsuited to access the subcycle nonlinear dynamics of a specimen in general. Consequently, it is highly desirable to achieve strong interaction between single electrons and atomic-scale excitations as a way to access their ultrafast nonlinear dynamics. In this context, the use of low-energy electrons with kinetic energies comparable to those of the quanta associated with the used optical fields opens a plausible avenue to overcome these challenges. The electron–light coupling strength increases when the electron energy is reduced, while a deviation from a classical-probe behavior is introduced by electron recoil (*43–45*). Low-energy electrons thus hold the potential to reveal new phenomena during their interaction with localized optical fields, a possibility that demands the exploration of physically relevant configurations.

Here, we reveal a wealth of previously unexplored quantum and recoil effects taking place during electron–light–matter interactions when the electron and photon energies are comparable.

Considering realistic frameworks that admit rigorous semi-analytical treatments, we theoretically explore electron–light interactions mediated by the scattering of light, electrons, or both at planar interfaces (Fig. 1). We adopt optical fields in the form of either externally incident plane waves or surface polaritons. Surface scattering leads to symmetry breaking that enhances the electron–light coupling, even allowing otherwise forbidden electron–photon interactions. In particular, we show that low-energy electrons can be inelastically scattered solely due to an evanescent optical field propagating along an electron-transparent surface (Fig. 1, A to C), including the emergence of a back-reflected electron signal (Fig. 1B). In addition, we demonstrate that a plane wave electron reflected on a light-transparent surface can produce inelastically reflected electrons because of the nonvanishing electron–photon coupling originating from translational symmetry breaking of the out-of-plane electron wave function (Fig. 1, D and E). The resulting reflected-electron spectrum exhibits substantial recoil effects (Fig. 1E). We further report on the possibility of reaching the strong electron–light coupling regime with moderate light intensities through Bragg scattering at planar atomic lattices, whereby the interaction is boosted under Rayleigh anomaly conditions (46, 47) dominated by lattice resonances (48), such that the interaction strength can diverge in analogy to lattice resonances when the lateral extension of the atomic lattice and the lateral coherence of electron and light beams are made arbitrarily large. Besides its interest from a fundamental viewpoint, the present study unveils exciting opportunities for improved microscopy and metrology in the regime of low-energy electrons exposed to optical fields of comparable photon energy. Our results are particularly relevant to the exploration of the rich phase and electronic-structure phenomenology exhibited by material surfaces, which are cornerstones in many technological applications.

RESULTS AND DISCUSSION

Theoretical framework for the interaction of low-energy electrons with light

We first consider a planar material acting through a one-dimensional (1D) potential $V(z)$ on the electron, while a generalization to laterally corrugated atomic lattices is presented further below. To study electron scattering by the planar structure in the presence of a classical optical field (e.g., light plane waves or surface polaritons), we write the Hamiltonian $\hat{\mathcal{H}}_0(\mathbf{r}) + \hat{\mathcal{H}}_1(\mathbf{r}, t)$, where $\hat{\mathcal{H}}_0(\mathbf{r}) = -\hbar^2 \nabla^2 / 2m_e + V(z)$ describes the electron–material system and $\hat{\mathcal{H}}_1(\mathbf{r}, t) = -(ie\hbar/m_e c)\, \mathbf{A}(\mathbf{r}, t) \cdot \nabla$ accounts for the electron–light interaction. The latter arises from the minimal coupling prescription applied to a classical vector potential $\mathbf{A}(\mathbf{r}, t)$ after neglecting A^2 terms and adopting a gauge in which the scalar potential is zero.

We focus on monochromatic fields of frequency ω and in-plane wave vector $\mathbf{k}_\parallel = (k_x, k_y)$, characterized by a vector potential $\mathbf{A}(\mathbf{r}, t) = \mathbf{A}(z)\, e^{i\mathbf{k}_\parallel \cdot \mathbf{R} - i\omega t} + \text{c. c.}$, where the notation $\mathbf{R} = (x, y)$ is adopted. Also, in the absence of illumination, the electron wave function is taken to
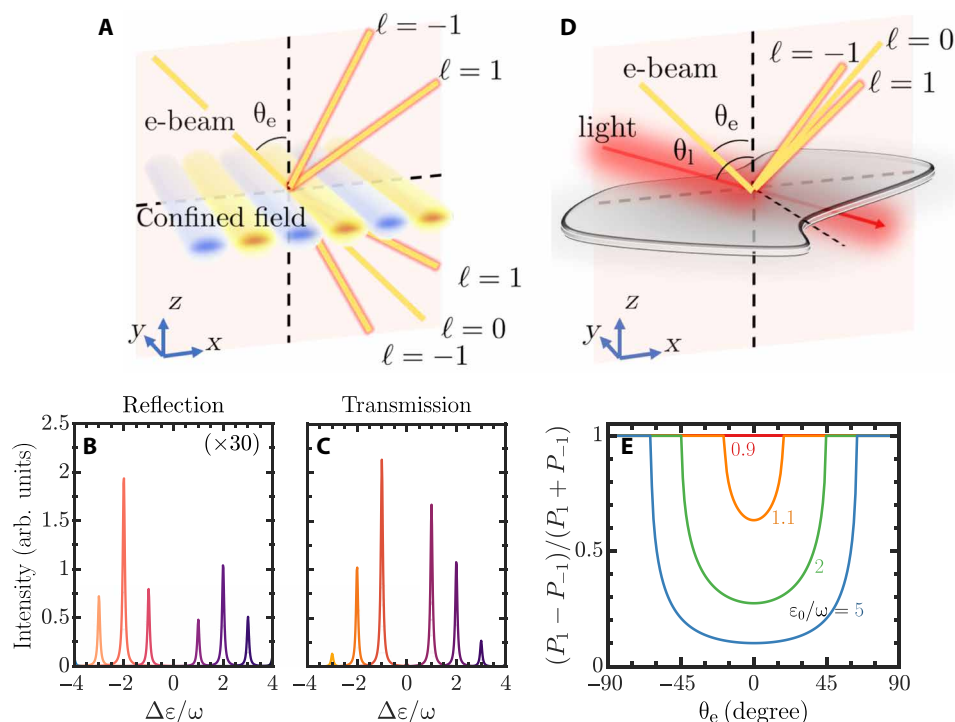
Fig. 1. Electron–light–matter interaction and recoil effects with low-energy electrons. (**A**) Illustration of inelastic electron scattering by the evanescent optical field associated with propagating surface polaritons. (**B** and **C**) Transmission (B) and reflection (C) electron spectra in the configuration of (A) for electrons of incident energy $\hbar\varepsilon_0 = 10$ eV and angle $\theta_e = 45°$ combined with polaritons of electric-field amplitude $E_0 = 6 \times 10^8$ V/m, effective refractive index $n_{eff} = 50$, and energy $\hbar\omega = 1$ eV. For readability, spectral peaks are broadened with a Lorentzian of 0.1 full width at half maximum (FWHM) in $\Delta\varepsilon/\omega$, with $\Delta\varepsilon = \varepsilon - \varepsilon_0$. (**D**) Nonvanishing interaction between a plane wave of light and an electron reflected on a light-transparent surface. (**E**) Despite the small coupling in (D) ($P_1 < 2\%$), strong recoil effects are observed for $\varepsilon_0 \sim \omega$ in the asymmetry factor $(P_1 - P_{-1})/(P_1 + P_{-1})$, which vanishes in the classical regime ($\varepsilon_0 \gg \omega$); we take $E_0 = 8 \times 10^7$ V/m, $\theta_e = 45°$, $\theta_l = 90°$, and $\hbar\omega = 1$ eV.

be a solution of the $\hat{\mathcal{H}}_0(\mathbf{r})$ Hamiltonian, namely, $\psi_0(\mathbf{r}, t) = \varphi_{00}(z)$ $e^{i\mathbf{q}_{0\parallel} \cdot \mathbf{R} - i\varepsilon_0 t}$, having a well-defined energy $\hbar\varepsilon_0$ and in-plane wave vector $\mathbf{q}_{0\parallel}(\perp \hat{\mathbf{z}})$. Now, in-plane translation symmetry and energy conservation allow us to write the perturbation series

$$\psi(\mathbf{r}, t) = \sum_{n=0}^{\infty} \sum_{\ell=-n}^{n} \varphi_{n\ell}(z)\, e^{i(\mathbf{q}_{0\parallel} + \ell\, \mathbf{k}_\parallel) \cdot \mathbf{R} - i(\varepsilon_0 + \ell\omega)t} \quad (1)$$

where n runs over scattering orders, while ℓ denotes the net number of exchanged photons (i.e., absorbed or emitted by the electron for $\ell > 0$ and $\ell < 0$, respectively). In addition, $\psi(\mathbf{r}, t)$ satisfies the Lippmann–Schwinger equation $\psi(\mathbf{r}, t) = \psi_0(\mathbf{r}, t) + \int d^3\mathbf{r}' \int dt'\, \mathcal{G}_0(\mathbf{r}, \mathbf{r}', t - t')\, \hat{\mathcal{H}}_1(\mathbf{r}', t')\, \psi(\mathbf{r}', t')$, where the Green function $\mathcal{G}_0(\mathbf{r}, \mathbf{r}', t - t')$ is defined by $[\hat{\mathcal{H}}_0(\mathbf{r}) - i\hbar\partial_t]\, \mathcal{G}_0(\mathbf{r}, \mathbf{r}', t - t') = -\delta(\mathbf{r} - \mathbf{r}')\delta(t - t')$. Combining these elements, we obtain the recurrence relation

$$\varphi_{n\ell}(z) = \frac{\hbar e}{m_e c} \int dz'\, \mathcal{G}_0(z, z', \varepsilon_\ell^\perp)$$
$$\times \Big\{ \mathbf{A}(z') \cdot [\mathbf{q}_{0\parallel} + (\ell-1)\, \mathbf{k}_\parallel - i\hat{\mathbf{z}}\, \partial_{z'}]\, \varphi_{n-1,\ell-1}(z') \quad (2)$$
$$+ \mathbf{A}^*(z') \cdot [\mathbf{q}_{0\parallel} + (\ell+1)\, \mathbf{k}_\parallel - i\hat{\mathbf{z}}\, \partial_{z'}]\, \varphi_{n-1,\ell+1}(z') \Big\}$$

for $n > 0$, where $\mathcal{G}_0(z, z', \varepsilon_\ell^\perp)$ is the frequency-domain 1D Green function satisfying $\mathcal{G}_0(\mathbf{r}, \mathbf{r}', t - t') = (2\pi)^{-3} \int d^2\mathbf{q}_\parallel \int d\varepsilon\, \mathcal{G}_0(z, z', \varepsilon)\, e^{i\mathbf{q}_\parallel \cdot (\mathbf{R} - \mathbf{R}') - i\varepsilon(t - t')}$, and we define $\varepsilon_\ell^\perp = \varepsilon_0 + \ell\omega - \hbar|\mathbf{q}_{0\parallel} + \ell\, \mathbf{k}_\parallel|^2 / 2m_e$, such that $\hbar\varepsilon_\ell^\perp$ is the out-of-plane electron energy after the exchange of a net number of photons ℓ (see section S1 for a self-contained derivation).

We consider planar structures of negligible thickness and expand the electron wave function components in Eq. 1 using the ansatz

$$\varphi_{n\ell}(z) = \sum_{s=\pm} \sum_j \alpha_{n\ell}^{js}\, e^{\zeta_{n\ell}^{js} z}\, \Theta(sz) \quad (3)$$

within the regions above ($s = +$) and below ($s = -$) the material. Here, j labels contributions that can be either evanescent ($\mathrm{Re}\{\zeta_{n\ell}^{j\pm}\} \neq 0$) or propagating (imaginary $\zeta_{n\ell}^{j\pm}$). Inserting Eq. 3 into Eq. 2, we find a recursive expression with a unique solution for the coefficients $\alpha_{n\ell}^{j\pm}$ and $\zeta_{n\ell}^{j\pm}$, which automatically satisfy the physical conditions $\mathrm{Re}\{\zeta_{n\ell}^{j+}\} \leq 0$ and $\mathrm{Re}\{\zeta_{n\ell}^{j-}\} \geq 0$ (see the Supplementary Materials). In addition, the purely propagating components have exponential coefficients $\zeta_{n\ell}^{j\pm} = \pm i q_{\ell z}$ (i.e., imaginary and independent of n and j), where $q_{\ell z} = \sqrt{2 m_e \varepsilon_\ell^\perp / \hbar}$ is determined by energy conservation for a net number of photon exchanges ℓ. Finally, the fractions of ℓ-resolved electrons scattered along the upward (+) and downward (−) directions are given by

$$P_\ell^\pm = \frac{q_{\ell z}}{q_{0z}} \left| {\sum_{nj}}' \alpha_{n\ell}^{j\pm} \right|^2 \quad (4)$$

where the primed sum indicates that it is restricted to purely propagating waves.

Recoil and quantum effects in surface-scattered electrons
Fully electron-reflecting surface

As a tutorial configuration, we first consider an electron with energy $\hbar\varepsilon_0$ and incident angle θ_e (with respect to the surface normal) that

undergoes total reflection at a planar surface supporting a surface polariton with in-plane wave vector $k_\parallel = |\mathbf{k}_\parallel| = n_{\mathrm{eff}} k$, where $k = \omega/c$ is the light wave vector and $n_{\mathrm{eff}} > 1$ is an effective index of refraction. For a thin metallic film of permittivity $\epsilon < 0$ and thickness d embedded in a medium of permittivity $\epsilon_s > 1$, we have $n_{\mathrm{eff}} = \epsilon_s \lambda / [\pi(1 - \epsilon)d]$ at a light wavelength λ, so thin films favor large values of n_{eff} [e.g., $n_{\mathrm{eff}} = 40$ for $\lambda = 500$ nm in currently available (49) 10-monolayer crystalline Ag(111) films deposited on Si]. Higher values of $n_{\mathrm{eff}} \sim 100$'s are displayed by infrared graphene plasmons (50, 51) and phonon polaritons in few-layer hexagonal boron nitride (hBN) (52, 53).

For simplicity, we take the electron and the surface polariton to share the same in-plane direction of incidence with $\mathbf{q}_{0\parallel} \parallel \mathbf{k}_\parallel \parallel \hat{\mathbf{x}}$, such that the associated vector potential can be written as $\mathbf{A}(\mathbf{r}) = (E_0/k)\, (\kappa^2 + k_\parallel^2)^{-1/2}\, (\kappa\, \hat{\mathbf{x}} + i\, k_\parallel\, \mathrm{sign}\{z\}\, \hat{\mathbf{z}})\, e^{i k_\parallel x - \kappa |z|}$, where E_0 is a global electric-field amplitude (see the Supplementary Materials). In addition, the electron–surface interaction is assumed to be elastic, and thus, any inelastic electron signal stems from surface-polariton emission and absorption processes by the electron. In this scenario, we can set the z component of the zeroth-order electron wave function as $\varphi_{00}(z) = [e^{-i q_{0z} z} - e^{i q_{0z} z}]\Theta(z)$, while the Green function in Eq. 2 reduces to $\mathcal{G}_0(z, z', \varepsilon_\ell^\perp) = (i m_e / \hbar^2 q_{\ell z})[e^{i q_{\ell z}(z + z')} - e^{i q_{\ell z}|z - z'|}]\Theta(z)\Theta(z')$ (see section S1). Inserting these elements into Eq. 2 and noticing that only reflected components need to be considered, we find a set of analytical coefficients $\alpha_{n\ell}^{j+}$ and $\zeta_{n\ell}^{j+}$, from which the reflection probability $P_\ell \equiv P_\ell^+$ for a given ℓ channel is obtained via Eq. 4.

It is instructive to examine the $\varepsilon_0 \gg \omega$ limit, where recoil effects should play a minor role. As a direct generalization of the result obtained for an electron moving with constant velocity along a straight-line trajectory (6), we approximate the ℓ-dependent inelastic probability as $P_\ell = J_\ell^2(2|\beta|)$, where $\beta = (ie/\hbar c) \int dt\, \dot{\mathbf{r}}_e(t) \cdot \mathbf{A}[\mathbf{r}_e(t)]\, e^{-i\omega t}$ is an electron–light coupling parameter obtained by integrating over time the vector potential component parallel to the velocity $\dot{\mathbf{r}}_e(t)$ and evaluated at the electron position $\mathbf{r}_e(t)$. Taking a specularly reflected trajectory with the surface-polariton field given above, we obtain

$$\beta = \frac{2i}{\sqrt{2 n_{\mathrm{eff}}^2 - 1}}\, \frac{e E_0 c}{\hbar\omega^2}\, \frac{(n_{\mathrm{eff}} c/v - \sin\theta_e)\cos\theta_e}{(c/v - n_{\mathrm{eff}} \sin\theta_e)^2 + (n_{\mathrm{eff}}^2 - 1)\cos^2\theta_e} \quad (5)$$

For reference, we note that the prefactor $eE_0 c/\hbar\omega^2$ takes a value of ≈ 2 for $E_0 = 10^7$ V/m and $\hbar\omega = 1$ eV. This mode energy is characteristic of surface plasmons in ultrathin metal films (49) and exciton polaritons in transition-metal dichalcogenides (54, 55), while polaritons of lower energy [e.g., $\hbar\omega \sim 0.1$ eV in graphene (50, 51) and hBN (52, 53)] should produce larger coupling for the same field amplitude in accordance to the scaling $\beta \propto 1/\omega^2$. Equation 5 reveals the important role of confinement in enhancing the electron–polariton coupling: Given a certain electron velocity v, the denominator reaches its minimum value under the condition

$$c/n_{\mathrm{eff}} = v\, \sin\theta_e \quad (6)$$

(i.e., when the surface-polariton phase velocity matches the in-plane projection of the electron velocity). In addition, Eq. 5 illustrates the well-known linear scaling of the coupling coefficient with the applied electric-field amplitude E_0.

Incidentally, we consider relatively high optical electric-field amplitudes (up to $E \sim 10^8$ V/m, corresponding to intensities $cE^2/2\pi > 10^{14}$ W/m^2), which are commonly used in ultrafast electron microscopy experiments during illumination with laser pulses of $\sim$100-fs duration (3, 56), such that the pulse fluence is below the damage threshold of the sampled nanostructures.

Figure 2 highlights the importance of recoil effects in the interaction between a low-energy electron and a strongly confined surface polariton by contrasting the classical nonrecoil PINEM theory (Fig. 2, A to D based on Eq. 5) with the rigorous quantum formalism introduced above (Fig. 2, E to H, and Eq. 4). For clarity, we stress that nonrecoil calculations are obtained by assuming a prescribed classical electron trajectory reflected at the surface with constant velocity, whereas recoil calculations involve a full quantum treatment of the system, including the change in electron velocity and nonspecular direction of reflection produced by polariton exchanges. As a first observation, the classical treatment in Eq. 5 provides the necessary conditions to reach a large electron–light coupling translated into substantial inelastic probabilities (Fig. 2, A to D). Focusing for concreteness on the $\ell = \pm 1$ channels (see the Supplementary Materials for more sidebands), the parameter space for which electron–light coupling is maximized is well captured by the classical framework, and it corresponds to the phase-matching condition in Eq. 6 (i.e., $\hbar\varepsilon_0 \approx m_e c^2 / 2n_{\text{eff}}^2 \sim 4$ eV with $\theta_e = 90°$), for which the coupling diverges as $\beta \propto 1/\cos\theta_e$ near $\theta_e = 90°$. However, both the intensity profile in the $(\varepsilon_0, \theta_e)$ phase space and the magnitude of the electron–light coupling strength are markedly different in the nonrecoil and recoil theories. Specifically, the incorporation of recoil in the latter leads to asymmetric loss–gain spectra (i.e., $P_{-\ell} \neq P_\ell$) and abrupt thresholds in P_ℓ (Fig. 2, E to G). These observations can be interpreted by noting that energy–momentum conservation imposes the condition $q_{\ell z} = q_0 \sqrt{1 + \ell\omega/\varepsilon_0 - |\sin\theta_e + \ell k_\parallel/q_0|^2}$, and thus, not only the emission ($\ell < 0$) and absorption ($\ell > 0$) probabilities are rendered different but also the inelastic signal vanishes whenever $1 + \ell\omega/\varepsilon_0 < |\sin\theta_e + \ell k_\parallel/q_0|^2$, since $q_{\ell z}$ becomes purely

imaginary (i.e., the corresponding electron wave is evanescent; see also fig. S1). Another notable consequence of recoil is the redistribution of probability to neighboring ℓ's near the aforementioned thresholds (see Fig. 2H), in contrast to the symmetric spectrum produced by the classical description (Fig. 2D). This behavior is less pronounced at lower values of θ_e (see fig. S2).

It should be noted that recoil imposes classical kinematic constraints relating incident and scattered electrons. In the present context, these constraints imply a change in the direction of motion and velocity of the electron when absorbing or emitting a certain number of photons. We remark that the resulting kinematic relations associated with recoil emerge naturally in our formalism, from which the associated probabilities P_ℓ are calculated following a self-contained quantum treatment of the system.

Partially electron-reflecting surface

We expect partial transmission and reflection when the electron is scattered by an atomically thin two-dimensional (2D) material, which we describe through a surface potential $V(z) = U_0 \, \delta(z)$. The parameter U_0 has units of energy times length, and arguing that an atomic monolayer can be described by a barrier of finite thickness $d \lesssim 1$ nm and internal potential V_0 in the electronvolt range, we expect $U_0 \approx V_0 d$ in the eV × nm range. We also assume the material to support long-lived polaritonic modes [e.g., phonon polaritons in hBN (52) or plasmons in doped graphene (51)], so that they are characterized by a real effective index n_{eff}. The calculation of the probabilities associated with the electron wave functions involved in the net exchange of ℓ polariton quanta follows the same steps as in the above scenario of full reflection, but now both reflected and transmitted electron components are produced. For an electron prepared with an incident $-q_{0z}$ wave vector in the out-of-plane direction, the wave function in the absence of illumination is given by $\varphi_{00}(z) = [e^{-iq_{0z}z} + r_0 e^{iq_{0z}z}]\Theta(z) + t_0 e^{-iq_{0z}z}\Theta(-z)$, where we use the transmission and reflection coefficients $t_\ell = (1 + imeU_0/\hbar^2 q_{\ell z})^{-1}$ and $r_\ell = t_\ell - 1$, respectively. We use this result together with the Green function $\mathcal{G}_0(z, z', \varepsilon_\ell^\perp) = -(im_e/\hbar^2 q_{\ell z})[e^{iq_{\ell z}|z-z'|} + r_\ell \, e^{iq_{\ell z}(|z|+|z'|)}]$ (see section S1) to obtain
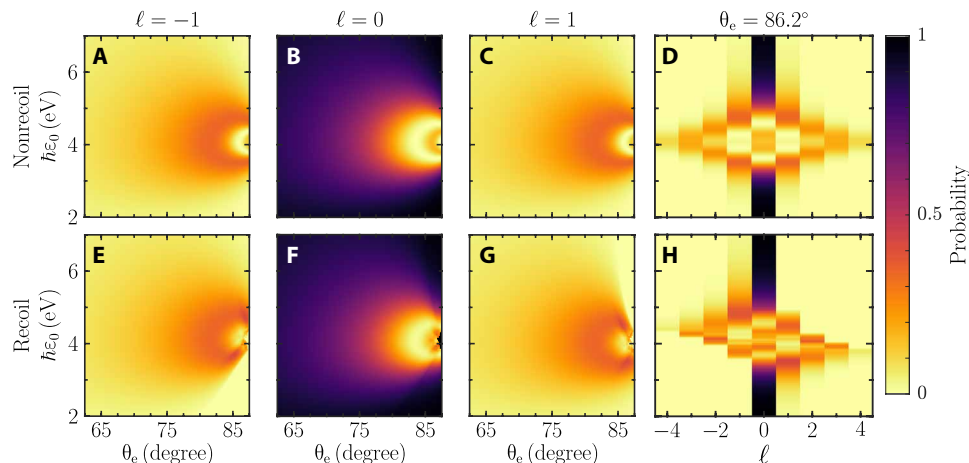
Fig. 2. Inelastic scattering of low-energy electrons upon total reflection at a polariton-supporting surface. (**A** to **C** and **E** to **G**) Probabilities corresponding to a net exchange of $\ell = 0, \pm 1$ quanta calculated without [(A) to (C)] and with [(E) to (G)] inclusion of quantum recoil as a function of electron incidence angle θ_e. (**D** and **H**) Electron spectra for $\theta_e = 86.2°$ obtained without (D) and with (H) recoil. We consider a polaritonic electric-field amplitude $E_0 = 5 \times 10^6$ V/m, effective refractive index $n_{\text{eff}} = 250$, and energy $\hbar\omega = 0.2$ eV.

the reflected and transmitted ℓ-resolved probabilities $P_\ell^\pm$ from Eq. 4 following the formalism developed above. The results are plotted as a function of electric-field amplitude for different electron energies and $U_0 = 1$ eV nm in Fig. 3 (see fig. S3 for $U_0 = 0$ results). Again, we find recoil effects emerging through strong asymmetries in the electron spectra, which, as anticipated, become more symmetric as the electron energy is increased toward the $\varepsilon_0 \gg \omega$ regime. However, strong asymmetries persist at high orders ℓ, and particularly Fig. 3 (G and H), which shows $|P_\ell - P_{-\ell}|/(P_\ell + P_{-\ell})$ as a function of incident electron energy for $\ell = 1 - 10$, reveals substantial asymmetries up to relatively high electron energies for values of ℓ increasing with ε_0. These results are qualitatively correct even when more involved z-dependent potentials are considered (e.g., finite-thickness films) because the Green function outside the material retains the same expression as above (57), with reflection and transmission coefficients depending on the details of the potential.

Nonvanishing interaction of surface-scattered electrons and unscattered light plane waves

An interesting scenario is presented when a thin film is illuminated from the far field, and the scattered optical components are comparatively negligible, so that the electron mainly sees an external light plane wave. Here, electron–light coupling can still take place under this configuration because the free-space energy–momentum mismatch is broken by the fact that the electron is scattered by the material. We regard this situation as the complementary of electron shaping mediated by PINEM interaction [i.e., SIELS assisted by electron-transparent, light-reflecting plates, in which the kinematic electron–photon free-space coupling mismatch is circumvented by having light half-plane waves instead of full plane waves (56)]. We note that 2D monolayers (e.g., graphene and hBN) are nearly

transparent to light [e.g., ~2.3% absorption by graphene over a wide spectral range (58, 59)] and can thus be regarded as good candidates to explore the interaction of light plane waves with surface-reflected low-energy electrons (i.e., when light scattering and absorption by the material is negligible, but the electron is partially reflected).

We explore this idea in Fig. 4, where the incident electron is considered to be fully reflected by the film, and it interacts with a freely propagating (i.e., negligibly scattered by the film) p-polarized light plane wave (i.e., with the optical magnetic field oriented parallel to the surface). The theoretical analysis of this configuration is analogous to that in Fig. 2 but using a plane-wave optical field instead of a surface mode. For simplicity, we limit the calculations to first order in the electron–light interaction under the assumption of low-enough optical-field intensities, thus generating $\ell = \pm 1$ sidebands only. Specifically, we present in Fig. 4 the resulting probabilities $P_{\ell=\pm 1}^\pm$ as a function of light and electron incidence angles, comparing nonrecoil and recoil (Eq. 4) descriptions. Incidentally, the coupling parameter in the former is given by

$$\beta = \frac{2eE_0 c}{\hbar \omega^2} \frac{\cos\theta_e(\sin\theta_l \, c/v - \sin\theta_e)}{(c/v - \sin\theta_l \sin\theta_e)^2 - \cos^2\theta_l \, \cos^2\theta_e}$$

where E_0 is the light-plane-wave amplitude. We find again that recoil leads to asymmetric inelastic electron signals, as well as regions of the (θ_l, θ_e) parameter space in which electron–light coupling becomes kinematically allowed or forbidden, accompanied by a transfer of probability to the symmetric ($\ell \rightarrow -\ell$) channel. In contrast to the interaction with surface polaritons, where phase matching at grazing incidence produced the strongest interaction, now phase matching is forbidden (i.e., the in-plane optical wave vector is always smaller than the in-plane electron wave vector), rendering the
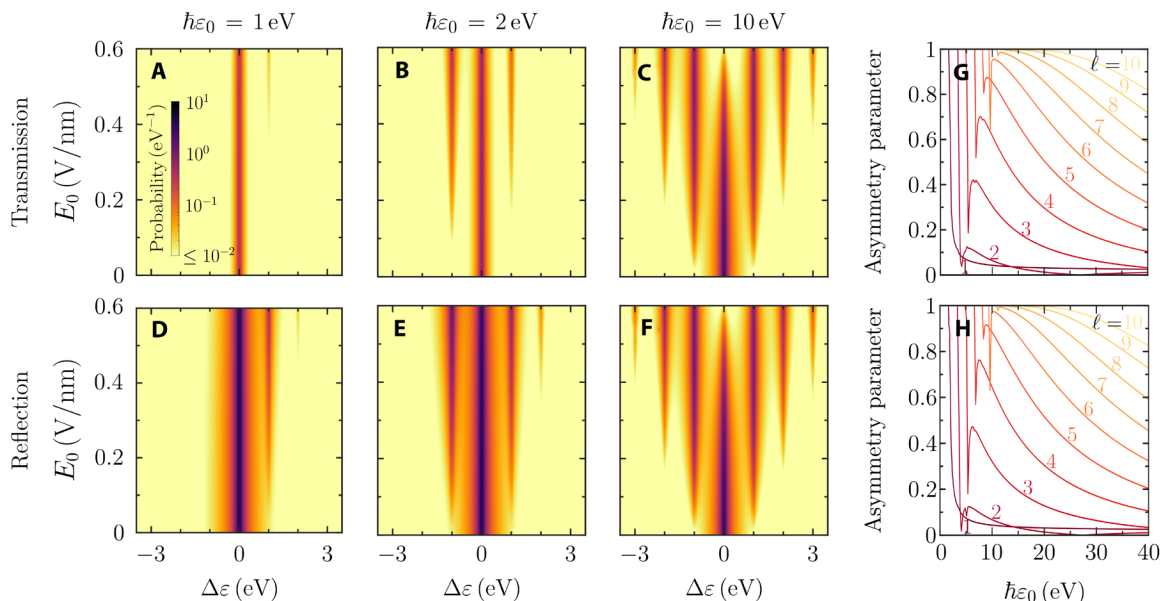
Fig. 3. Inelastic scattering of low-energy electrons upon partial reflection at a polariton-supporting thin film. (**A** to **F**) We show transmitted [(A) to (C)] and reflected [(D) to (F)] electron spectra as a function of polaritonic electric-field amplitude E_0 for fixed effective refractive index ($n_{eff} = 50$) and energy ($\hbar\omega = 1$ eV). Selected incident electron energies $\hbar\varepsilon_0$ are considered, while the incidence angle is fixed at $\theta_e = 45°$. Spectral features are broadened by a Lorentzian of 0.1 eV FWHM. (**G** and **H**) Asymmetry parameter associated with the exchange of ℓ photons, $|P_\ell - P_{-\ell}|/(P_\ell + P_{-\ell})$, as a function of electron energy for a field amplitude $E_0 = 2 \times 10^8$ V/m in the transmitted (G) and reflected (H) electron components. Electron-surface scattering is modeled through a δ-function potential of amplitude $U_0 = 1$ eV nm in all cases.

coupling smaller. The maximum coupling is observed at grazing light incidence ($\theta_l = \pm 90°$) and normal electron incidence ($\theta_e = 0°$), which is consistent with the angular scaling of the classical coupling coefficient as $\beta \propto \sin\theta_l \cos\theta_e$ for $v \ll c$. These conditions guarantee
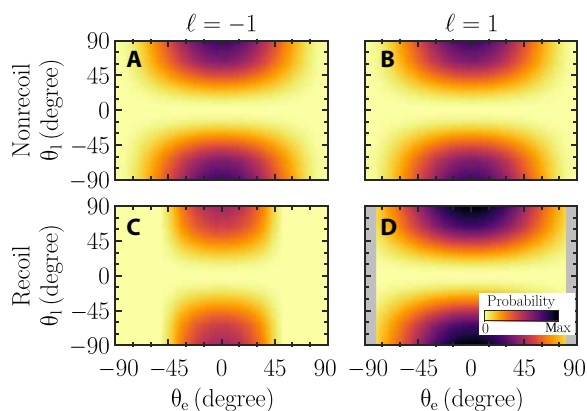

Fig. 4. Inelastic interaction between a light plane wave and surface-scattered electrons. We plot the probability associated with $\ell = \pm 1$ net photon exchanges as a function of the electron (θ_e) and photon (θ_l) incidence angles without (**A** and **B**) and with (**C** and **D**) inclusion of recoil for an electron-opaque, light-transparent surface. We assume total electron reflection and take $\hbar\varepsilon_0 = 2$ eV, $E_0 = 8 \times 10^7$ V/m, and $\hbar\omega = 1$ eV. In (**D**), kinematically forbidden regions are shaded in gray.

maximum overlap of the light electric field along the electron trajectory.

Light-assisted low-energy electron diffraction

Low-energy electrons with energies ∼10 to 500 eV are commonly used to study the atomic structure of crystal surfaces in low-energy electron diffraction (LEED) (60–62) because they penetrate only a few atomic layers and have de Broglie wavelengths commensurate with the atomic spacings. In a related context, energy-resolved inelastic low-energy electron surface scattering is also used to probe surface modes (63–65), while ultrafast LEED grants one access to time-resolved structural dynamics (66, 67). Here, we theoretically study the interaction of surface-diffracted electrons with light plane waves and show the important role played by recoil in the underlying electron–light coupling, including the presence of lattice resonances that boost the interaction under Rayleigh anomaly conditions (46).

To illustrate electron–light–matter interactions in the presence of Bragg diffraction, we consider a low-energy electron normally impinging on an illuminated monolayer of gold atoms arranged in a (111) triangular lattice with an Au–Au bond distance of 0.288 nm (Fig. 5A). In the absence of external illumination, the diffracted electron wave function consists of components with wave vectors given by $\mathbf{q}_{\mathbf{G}0}^{\pm} = \mathbf{G} \pm \sqrt{q_0^2 - G^2}\,\hat{\mathbf{z}}$, where $\mathbf{G}$ are 2D reciprocal lattice vectors, while the + (−) sign corresponds to upward (downward)
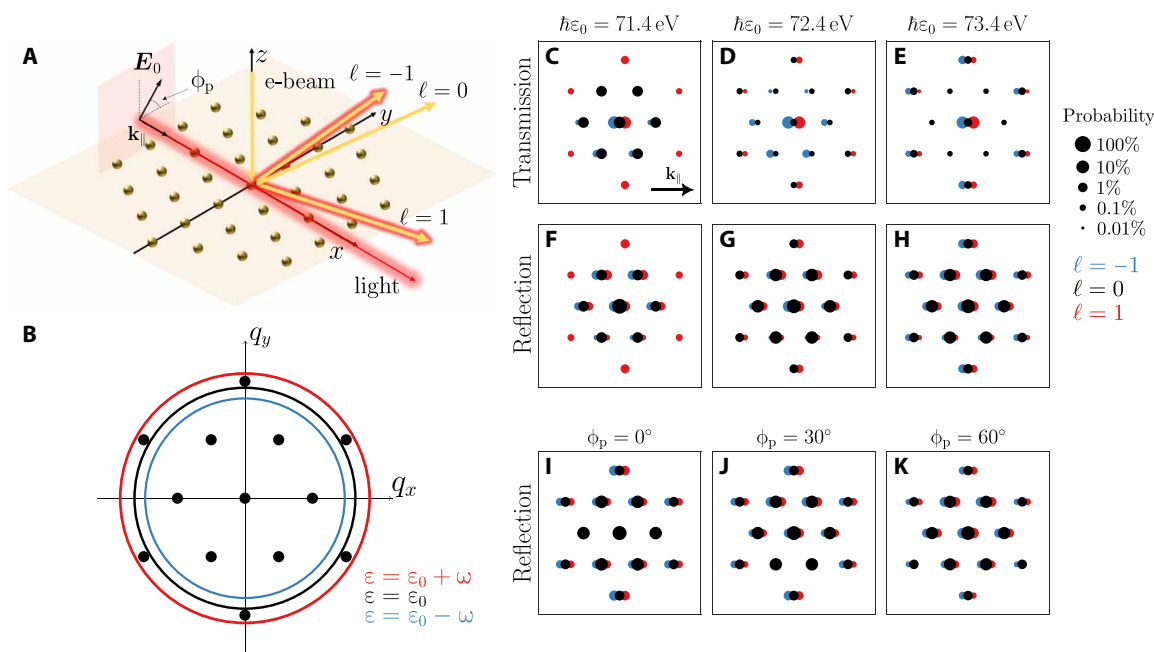
Fig. 5. Recoil effects in the interaction of light with lattice-diffracted electrons. (**A**) We consider a normally incident electron undergoing diffraction by an Au(111) monolayer (Au–Au distance $d \approx 0.2884$ nm, with atomic bonds along y) under grazing plane-wave light irradiation along x ($\mathbf{k}_\| \| \hat{\mathbf{x}}$) with linear polarization in the y-z plane as indicated by the angle ϕ_p. Each of the electron Bragg diffraction orders (see yellow arrows for one of them) splits in energy and direction of reflection/transmission upon exchange of a net number of photons ℓ. (**B**) Electron isoenergy contours after exchanging $\ell = -1$, 0, and 1 photons (blue, black, and red circles), superimposed on the reciprocal lattice of the atomic monolayer ($4\pi/\sqrt{3}d$ distance between sites). We consider 71.4-eV incident electrons and 1-eV photons. (**C** to **H**) Intensity of transmitted [(C) to (E)] and reflected [(F) to (H)] Bragg peaks for three different incident electron energies {see labels above [(C) and (F)], [(D) and (G)], and [(E) and (H)]} upon exchange of $\ell = -1$, 0, or 1 photons (1-eV energy). The light wave vector $\mathbf{k}_\|$ is indicated in (C), and the electric-field amplitude is $E_0 = 2.5 \times 10^8$ V/m with polarization set by $\phi_p = 45°$. The area of the circles gives the fraction of electrons in each Bragg peak (see log scale legend). (**I** to **K**) Same as (E), but for varying polarization angles ϕ_p (see top labels).

electron motion relative to the atomic plane. Lattice scattering is elastic, so all of these wave vectors have a magnitude $q_0 = \sqrt{2m_e \varepsilon_0 / \hbar}$ determined by the incident electron energy $\hbar\varepsilon_0$. Diffracted electron plane waves with $G < q_0$ generate observable LEED spots, as determined by an Ewald sphere construction (see Fig. 5), whereas waves with $G > q_0$ are evanescent. The latter do not explicitly contribute to the far-field electron scattering probability, but they have to be retained in the description of dynamical electron diffraction by the atomic layer (*60–62*). Starting from a normally incident electron, the wave function associated with the incident and scattered waves in the absence of illumination takes the form

$$\psi_0(\mathbf{r}, t) = \left[e^{-iq_0 z} + \sum_\pm B_\mathbf{G}^\pm e^{i\mathbf{q}_{\mathbf{G}0}^\pm \cdot \mathbf{r}} \Theta(\pm z) \right] e^{-i\varepsilon_0 t} \qquad (7A)$$

where $B_\mathbf{G}^\pm$ are scattering amplitudes.

Upon interaction with an incident light plane wave of wave vector $\mathbf{k}$, every diffraction order (either propagating or evanescent) can exchange energy with the light field in multiples of the photon energy and in-plane wave vector (i.e., $\ell\hbar\omega$, and $\ell\mathbf{k}_\parallel$, respectively), giving rise to diffracted components with wave vectors $\mathbf{q}_{\mathbf{G}\ell}^\pm = \mathbf{G} + \ell\mathbf{k}_\parallel \pm q_{\mathbf{G}\ell z}\hat{\mathbf{z}}$, where $q_{\mathbf{G}\ell z} = \sqrt{2m_e(\varepsilon_0 + \ell\omega)/\hbar - |\mathbf{G} + \ell\mathbf{k}_\parallel|^2}$, labeled by the direction of motion (+/− for upward/downward scattering) and the net lattice and photon momentum exchanges ($\hbar\mathbf{G}$ and $\ell\hbar\mathbf{k}_\parallel$). The total electron wave function takes the form

$$\psi(\mathbf{r}, t) = \left[e^{-iq_0 z} + \sum_\pm C_{\mathbf{G}\ell}^\pm e^{i\mathbf{q}_{\mathbf{G}\ell}^\pm \cdot \mathbf{r} - i\ell\omega t} \Theta(\pm z) \right] e^{-i\varepsilon_0 t} \qquad (7B)$$

where the amplitudes $C_{\mathbf{G}\ell}^\pm$ are self-consistently determined from an extension of LEED theory to incorporate the interaction with both the atomic lattice and the optical field (see the section S2 for details, including analytical expressions for the coefficients $B_\mathbf{G}^\pm$ and $C_{\mathbf{G}\ell}^\pm$ in Eqs. 7A and 7B, respectively). For simplicity, we limit our analysis to first order in the electron–light interaction, but we incorporate the interaction with the lattice to all orders.

As the electron energy increases, the number of diffracted spots also increases because more points are inside the Ewald sphere. In the elastic part ($\ell = 0$), a given diffraction order $\mathbf{G}$ is observed in the LEED pattern when the electron energy exceeds a threshold energy $\hbar^2 G^2 / 2m_e$. However, in the inelastic components, the changes in electron energy and momentum enter the condition for far-field propagation. For example, after exchanging ℓ photons, a previously evanescent order may become propagating if $\hbar|\mathbf{G} + \ell\mathbf{k}_\parallel|^2/2m_e < \varepsilon_0 + \ell\omega$, and likewise, a propagating Bragg-diffracted beam may become evanescent (Fig. 5B). These effects are more relevant when $\varepsilon_0 \sim \hbar G^2/2m_e$. In addition, electrons scattered at the onset of a diffraction order move under grazing conditions, so they spend more time near the surface and, therefore, undergo a stronger interaction with light. Consequently, by choosing the electron energy close to the threshold of one of the $\mathbf{G}$ beams, we expect to increase the coupling of diffracted electrons to light, emphasizing the importance of recoil (see below).

This phenomenology is illustrated in the calculations presented in Fig. 5 (C to H) for three different incident electron energies (in separate columns) near the threshold of the (1,1) and its symmetry-equivalent diffraction spots. We show the intensities of transmitted (Fig. 5, C to E) and reflected (Fig. 5, F to H) beams. Following the conditions under which a maximum electron–light interaction was observed in Fig. 4, we take the electron to be normally impinging on

the atomic plane, while a light plane wave is incident parallel to the x surface direction with linear polarization as indicated in Fig. 5A. The atomic lattice is oriented with Au–Au bonds along y. Upon inspection of our numerical results, we estimate an overall inelastic scattering probability of ~10 to 20% for incident electron energies up to 50 eV and optical electric-field strengths $E_0 \sim 2.5 \times 10^8$ V/m. In addition, we find that the waves corresponding to $\ell = \pm 1$ typically have comparable intensities to the transmitted $\ell = 0$ beam. In contrast to the amplitude found when adopting the nonrecoil approximation, which only depends on the amplitude of each $\mathbf{G}$-dependent LEED spot and its multiplexing into different energy sidebands according to the corresponding electron–light coupling coefficient β (i.e., considering the time integral of the field along the classical incoming and Bragg-reflected electron paths), a full quantum treatment including recoil reveals that all diffraction orders (propagating and evanescent) can contribute.

The onset of a new diffraction order during the scattering of waves by a periodic structure causes an anomaly consisting of the depletion of the specularly reflected and directly transmitted beams, as pointed out by Lord Rayleigh in the context of light diffraction by periodic gratings (*46–48*). In light-assisted inelastic electron diffraction, a related anomaly takes place when a scattered beam becomes grazing (i.e., a vanishing out-of-plane wave vector component $q_{\mathbf{G}\varepsilon_\ell z} = 0$ for a combination of reciprocal lattice vector $\mathbf{G}$ and sideband order ℓ or, equivalently, $\hbar\varepsilon_0 + \ell\hbar\omega = (\hbar^2/2m_e)|\mathbf{G} + \ell\mathbf{k}_\parallel|^2$ under normal electron-incidence conditions). Upon examination of the corresponding coefficients $C_{\mathbf{G}\ell}^\pm$ in Eq. 7B (see section S2), considering $q_{\mathbf{G}\varepsilon_\ell z} \approx 0$ and taking the field amplitude $\mathbf{E}_0 \perp \hat{\mathbf{z}}$ for simplicity, we can approximate

$$C_{\mathbf{G},\ell}^\pm \approx \frac{i^\ell e}{\hbar\omega} \frac{\mathbf{E}_0 \cdot \mathbf{G}}{q_{\mathbf{G}\varepsilon_\ell z} \, q_{\mathbf{G}\varepsilon_0 z}} \left(B_\mathbf{G}^+ + B_\mathbf{G}^- \right) \qquad (8)$$

and consequently, the probability $|C_{\mathbf{G},\ell}^\pm|^2$ diverges as $1/q_{\mathbf{G}\varepsilon_\ell z}^2$. An illustrative example is presented in Fig. 6 when varying either the electron energy (Fig. 6A) or the photon energy (Fig. 6B) around the conditions for the grazing emission of an inelastic electron beam. A divergence in the probability calculated to the first order of interaction with the light is observed, leading to unphysical values above unity. This indicates that the system enters into the nonperturbative regime, not only requiring higher orders of interaction to describe the system but also revealing that strong electron–light coupling can be reached even for small light intensities. Such a strong interaction results from in-phase scattering by a large number of atoms in the planar lattice, which demands the use of sufficiently wide electron and light beams (along lateral directions) that can be regarded as coherent plane waves over a large surface area. This divergence is well captured by Eq. 8 (Fig. 6, dashed-blue curves), in reasonable agreement with our rigorous first-order results (Fig. 6, solid-blue curves, obtained from eq. S23). We note that, in addition to the explicit $1/\omega$ factor in Eq. 8, the inelastic scattering coefficient $C_{\mathbf{G},\ell}^\pm$ is dominated by a $1/(q_{\mathbf{G}\varepsilon_\ell z} - q_{\mathbf{G}\varepsilon_0 z})$ term in eq. S23, thus resulting in an overall $\propto 1/\omega^4$ scaling of the probability with decreasing photon frequency ω, as indicated in Fig. 6B.

Concluding remarks

In summary, based on a comprehensive theoretical treatment of the quantum-mechanical interaction between low-energy free electrons
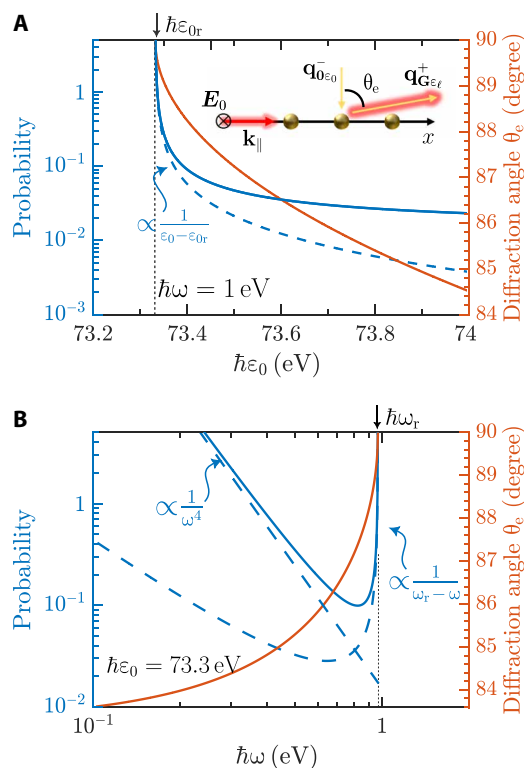
Fig. 6. Strong coupling between light and diffracted electrons. (**A**) Probability (blue curves, to first order) and azimuthal outgoing angle (orange curve) of the (2,1) diffraction spot [$\mathbf{G} = (2\pi/d)(\sqrt{3}\hat{\mathbf{x}} - \hat{\mathbf{y}})$] after emitting one photon ($\ell = -1$) as a function of electron energy $\hbar\varepsilon_0$ under the configuration of Fig. 5A for a light plane wave impinging along x with polarization along y, amplitude $E_0 = 2.5 \times 10^7$ V/m, and photon energy $\hbar\omega = 1$ eV. Rigorous first-order theory (solid blue curve) is compared with the analytical approximation in Eq. 8 (dashed curve). A divergent probability is observed when the inelastically diffracted beam becomes grazing at an electron energy $\hbar\varepsilon_{0r} \approx \hbar^2 G^2 / 2m_e + \hbar\omega \approx 73.3$ eV. (**B**) Same as (A), but shown as a function of photon energy for an incident electron energy $\hbar\varepsilon_0 = 73.3$ eV. The outgoing electron is grazing and the probability diverges at a photon energy $\hbar\omega_r \approx 1$ eV. The probability also diverges at low frequencies with the asymptotic behavior $\propto 1/\omega^4$ indicated by the dotted blue curve in (B).

and optical fields with comparable photon energies, we have identified a plethora of recoil and quantum effects emerging in the form of substantial modifications in the energy and angular distribution of electrons undergoing elastic surface scattering and inelastic interaction with optical fields associated with either surface polaritons or propagating light. In particular, we have shown that free electrons interacting with evanescent optical fields can undergo classically forbidden backscattering for a fully electron-transparent film. Furthermore, the interaction between surface-scattered electrons and unscattered light plane waves renders a nonzero electron–light coupling due to the breaking of translational symmetry in the electron wave function; we propose that suspended atomically thin layers may provide suitable conditions (high transparency to light and large electron scattering) to observe this effect.

As a common element in the interaction between free electrons and crystal surfaces, we have incorporated Bragg diffraction, which leads to an interplay between scattering by the atomic lattice and inelastic photon exchanges. The latter can transform propagating

diffraction orders into evanescent or the other way around. Strong electron–light coupling is predicted at the onset of an inelastically scattering electron beam, capitalizing on the in-phase interaction with many atoms in the structure. By strong coupling we refer to the fact that, for a given light intensity, the probability that the electron undergoes inelastic scattering can be made arbitrarily high, provided we are close enough to a lattice resonance, and the light and electron beams have a sufficiently large degree of lateral coherence. In practice, imperfections in the atomic lattice and atomic vibrations can reduce the strength of the divergence, so future work is needed to determine the ultimate limits of interaction boosted by lattice divergences and whether the strong-coupling regime can be reached down to the single-electron–single-photon level. This effect could be leveraged to optically shape free electrons using moderate light intensities, potentially operating in the continuous-wave regime without damaging the scattering material.

Although we have focused on planar surfaces, the concept of combining elastic scattering of low-energy electrons by a material structure and the inelastic interaction with light of comparably low photon energy is more general and could involve the use of nonperiodic nanostructures such as holes, tips, and other curved elements to guide and reshape the electron wave function and also increase or spatially modulate its interaction with specific optical modes. In a related context, electron interaction with illuminated atoms in the gas phase has a long tradition [42, 68–70], which could be revisited as a platform to optically modulate electrons and explore new physics. The novel directions opened by the presented theory and simulations could be experimentally explored in currently available low-energy electron-microscope setups.

Supplementary Materials

This PDF file includes:
Supplementary Text S1 and S2
Figs. S1 to S3
References

REFERENCES AND NOTES

1. B. Barwick, D. J. Flannigan, A. H. Zewail, Photon-induced near-field electron microscopy. *Nature* **462**, 902–906 (2009).
2. D. J. Flannigan, A. H. Zewail, 4D electron microscopy: Principles and applications. *Acc. Chem. Res.* **45**, 1828–1839 (2012).
3. A. Feist, K. E. Echternkamp, J. Schauss, S. V. Yalunin, S. Schäfer, C. Ropers, Quantum coherent optical phase modulation in an ultrafast transmission electron microscope. *Nature* **521**, 200–203 (2015).
4. B. Barwick, A. H. Zewail, Photonics and plasmonics in 4D ultrafast electron microscopy. *ACS Photonics* **2**, 1391–1402 (2015).
5. A. Polman, M. Kociak, F. J. García de Abajo, Electron-beam spectroscopy for nanophotonics. *Nat. Mater.* **18**, 1158–1171 (2019).
6. F. J. García de Abajo, V. Di Giulio, Optical excitations with electron beams: Challenges and opportunities. *ACS Photonics* **8**, 945–974 (2021).
7. C. Roques-Carmes, S. E. Kooi, Y. Yang, N. Rivera, P. D. Keathley, J. D. Joannopoulos, S. G. Johnson, I. Kaminer, K. K. Berggren, M. Soljačić, Free-electron-light interactions in nanophotonics. *Appl. Phys. Rev.* **10**, 011303 (2023).
8. F. J. García de Abajo, C. Ropers, Spatiotemporal electron beam focusing through parallel interactions with shaped optical fields. *Phys. Rev. Lett.* **130**, 246901 (2023).
9. F. J. García de Abajo, A. Asenjo-Garcia, M. Kociak, Multiphoton absorption and emission by interaction of swift electrons with evanescent light fields. *Nano Lett.* **10**, 1859–1863 (2010).
10. S. T. Park, M. Lin, A. H. Zewail, Photon-induced near-field electron microscopy (PINEM): Theoretical and experimental. *New J. Phys.* **12**, 123028 (2010).
11. L. Piazza, T. T. A. Lummen, E. Quiñonez, Y. Murooka, B. W. Reed, B. Barwick, F. Carbone, Simultaneous observation of the quantization and the interference pattern of a plasmonic near-field. *Nat. Commun.* **6**, 6407 (2015).

12. T. T. A. Lummen, R. J. Lamb, G. Berruto, T. LaGrange, L. Dal Negro, F. J. García de Abajo, D. McGrouther, B. Barwick, F. Carbone, Imaging and controlling plasmonic interference fields at buried interfaces. *Nat. Commun.* **7**, 13156 (2016).

13. G. M. Vanacore, I. Madan, F. Carbone, Spatio-temporal shaping of a free-electron wave function via coherent light-electron interaction. *Riv. Nuovo Cimento* **43**, 567–597 (2020).

14. Y. Kurman, R. Dahan, H. H. Sheinfux, K. Wang, M. Yannai, Y. Adiv, O. Reinhardt, L. H. G. Tizei, S. Y. Woo, J. Li, J. H. Edgar, M. Kociak, F. H. L. Koppens, I. Kaminer, Spatiotemporal imaging of 2D polariton wave packet dynamics using free electrons. *Science* **372**, 1181–1186 (2021).

15. D. Nabben, J. Kuttruff, L. Stolz, A. Ryabov, P. Baum, Attosecond electron microscopy of sub-cycle optical dynamics. *Nature* **619**, 63–67 (2023).

16. J. H. Gaida, H. Lourenço-Martins, M. Sivis, T. Rittmann, A. Feist, F. J. García de Abajo, C. Ropers, Attosecond electron microscopy by free-electron homodyne detection. *Nat. Photon.* **18**, 509–515 (2024).

17. T. Bucher, H. Nahari, H. H. Sheinfux, R. Ruimy, A. Niedermayr, R. Dahan, Q. Yan, Y. Adiv, M. Yannai, J. Chen, Y. Kurman, S. T. Park, D. J. Masiel, E. Janzen, J. H. Edgar, F. Carbone, G. Bartal, S. Tsesses, F. H. L. Koppens, G. M. Vanacore, I. Kaminer, Coherently amplified ultrafast imaging in a free-electron interferometer. arXiv:2305.04877 [physics.optics] (8 May 2023).

18. V. Di Giulio, M. Kociak, F. J. García de Abajo, Probing quantum optical excitations with fast electrons. *Optica* **6**, 1524–1534 (2019).

19. R. Dahan, A. Gorlach, U. Haeusler, A. Karnieli, O. Eyal, P. Yousefi, M. Segev, A. Arie, G. Eisenstein, P. Hommelhoff, I. Kaminer, Imprinting the quantum statistics of photons on free electrons. *Science* **373**, eabj7128 (2021).

20. Y. Yang, J.-W. Henke, A. S. Raja, F. Jasmin Kappert, G. Huang, G. Arend, Z. Qiu, A. Feist, R. N. Wang, A. Tusnin, A. Tikan, C. Ropers, T. J. Kippenberg, Free-electron interaction with nonlinear optical states in microresonators. *Science* **383**, 168–173 (2024).

21. K. E. Priebe, C. Rathje, S. V. Yalunin, T. Hohage, A. Feist, S. Schäfer, C. Ropers, Attosecond electron pulse trains and quantum state reconstruction in ultrafast transmission electron microscopy. *Nat. Photon.* **11**, 793–797 (2017).

22. M. Kozák, N. Schönenberger, P. Hommelhoff, Ponderomotive generation and detection of attosecond free-electron pulse trains. *Phys. Rev. Lett.* **120**, 103203 (2018).

23. Y. Morimoto, P. Baum, Diffraction and microscopy with attosecond electron pulse trains. *Nat. Phys.* **14**, 252–256 (2018).

24. G. M. Vanacore, G. Berruto, I. Madan, E. Pomarico, P. Biagioni, R. J. Lamb, D. McGrouther, O. Reinhardt, I. Kaminer, B. Barwick, H. Larocque, V. Grillo, E. Karimi, F. J. García de Abajo, F. Carbone, Ultrafast generation and control of an electron vortex beam via chiral plasmonic near fields. *Nat. Mater.* **18**, 573–579 (2019).

25. A. Konecná, F. J. García de Abajo, Electron beam aberration correction using optical near fields. *Phys. Rev. Lett.* **125**, 030801 (2020).

26. F. J. García de Abajo, A. Konecná, Optical modulation of electron beams in free space. *Phys. Rev. Lett.* **126**, 123901 (2021).

27. I. Madan, V. Leccese, A. Mazur, F. Barantani, T. LaGrange, A. Sapozhnik, P. M. Tengdin, S. Gargiulo, E. Rotunno, J.-C. Olaya, I. Kaminer, V. Grillo, F. J. García de Abajo, F. Carbone, G. M. Vanacore, Ultrafast transverse modulation of free electrons by interaction with shaped optical fields. *ACS Photonics* **9**, 3215–3224 (2022).

28. M. C. C. Mihaila, P. Weber, M. Schneller, L. Grandits, S. Nimmrichter, T. Juffmann, Transverse electron-beam shaping with light. *Phys. Rev. X* **12**, 031043 (2022).

29. T. E. Glover, R. W. Schoenlein, A. H. Chin, C. V. Shank, Observation of laser assisted photoelectric effect and femtosecond high order harmonic radiation. *Phys. Rev. Lett.* **76**, 2468–2471 (1996).

30. G. Saathoff, L. Miaja-Avila, M. Aeschlimann, M. M. Murnane, H. C. Kapteyn, Laser-assisted photoemission from surfaces. *Phys. Rev. A* **77**, 022903 (2008).

31. C. A. Arrell, J. Ojeda, L. Mewes, J. Grilj, F. Frassetto, L. Poletto, F. van Mourik, M. Chergui, Laser-assisted photoelectric effect from liquids. *Phys. Rev. Lett.* **117**, 143001 (2016).

32. S. V. Yalunin, M. Gulde, C. Ropers, Strong-field photoemission from surfaces: Theoretical approaches. *Phys. Rev. B* **84**, 195426 (2011).

33. P. Dombi, Z. Pápa, J. Vogelsang, S. V. Yalunin, M. Sivis, G. Herink, S. Schäfer, P. Gross, C. Ropers, C. Lienau, Strong-field nano-optics. *Rev. Mod. Phys.* **92**, 025003 (2020).

34. X. M. Bendaña, A. Polman, F. J. García de Abajo, Single-Photon generation by electron beams. *Nano Lett.* **11**, 5099–5103 (2011).

35. O. Kfir, H. Lourenço-Martins, G. Storeck, M. Sivis, T. R. Harvey, T. J. Kippenberg, A. Feist, C. Ropers, Controlling free electrons with optical whispering-gallery modes. *Nature* **582**, 46–49 (2020).

36. K. Wang, R. Dahan, M. Shentcis, Y. Kauffmann, A. Ben Hayun, O. Reinhardt, S. Tsesses, I. Kaminer, Coherent interaction between free electrons and a photonic cavity. *Nature* **582**, 50–54 (2020).

37. R. Dahan, S. Nehemia, M. Shentcis, O. Reinhardt, Y. Adiv, X. Shi, O. Beer, M. H. Lynch, Y. Kurman, K. Wang, I. Kaminer, Resonant phase-matching between a light wave and a free-electron wavefunction. *Nat. Phys.* **16**, 1123–1131 (2020).

38. J.-W. Henke, A. Sajid Raja, A. Feist, G. Huang, G. Arend, Y. Yang, F. J. Kappert, R. Ning Wang, M. Möller, J. Pan, J. Liu, O. Kfir, C. Ropers, T. J. Kippenberg, Integrated photonics enables continuous-beam electron phase modulation. *Nature* **600**, 653–658 (2021).

39. S. Tsesses, G. Bartal, I. Kaminer, Light generation via quantum interaction of electrons with periodic nanostructures. *Phys. Rev. A* **95**, 013832 (2017).

40. S. Huang, R. Duan, N. Pramanik, J. S. Herrin, C. Boothroyd, Z. Liu, L. J. Wong, Quantum recoil in free-electron interactions with atomic lattices. *Nat. Photon.* **17**, 224–230 (2023).

41. D. A. Varshalovich, M. I. D'yakonov, Quantum theory of modulation of an electron beam at optical frequencies. *Sov. Phys. Usp.* **33**, 51–57 (1971).

42. A. Weingartshofer, J. K. Holmes, G. Caudle, E. M. Clarke, H. Krüger, Direct observation of multiphoton processes in laser-induced free-free transitions. *Phys. Rev. Lett.* **39**, 269–270 (1977).

43. N. Talebi, Electron-light interactions beyond the adiabatic approximation: Recoil engineering and spectral interferometry. *Adv. Phys. X* **3**, 1499438 (2018).

44. N. Talebi, Strong interaction of slow electrons with near-field light visited from first principles. *Phys. Rev. Lett.* **125**, 080401 (2020).

45. F. J. García de Abajo, E. J. C. Dias, V. Di Giulio, Complete excitation of discrete quantum systems by single free electrons. *Phys. Rev. Lett.* **129**, 093401 (2022).

46. L. Rayleigh, On the dynamical theory of gratings. *Proc. R. Soc. Lond. A* **79**, 399–416 (1907).

47. L. Rayleigh, III. Note on the remarkable case of diffraction spectra described by Prof. Wood. *Philos. Mag.* **14**, 60–65 (1907).

48. F. J. García de Abajo, Colloquium: Light scattering by particle and hole arrays. *Rev. Mod. Phys.* **79**, 1267–1290 (2007).

49. Z. M. Abd El-Fattah, V. Mkhitaryan, J. Brede, L. Fernández, C. Li, Q. Guo, A. Ghosh, A. Rodríguez Echarri, D. Naveh, F. Xia, J. E. Ortega, F. J. García de Abajo, Plasmonics in atomically thin crystalline silver films. *ACS Nano* **13**, 7771–7779 (2019).

50. A. Woessner, M. B. Lundeberg, Y. Gao, A. Principi, P. AlonsoGonzález, M. Carrega, K. Watanabe, T. Taniguchi, G. Vignale, M. Polini, J. Hone, R. Hillenbrand, F. H. L. Koppens, Highly confined low-loss plasmons in graphene-boron nitride heterostructures. *Nat. Mater.* **14**, 421–425 (2015).

51. G. X. Ni, A. S. McLeod, Z. Sun, L. Wang, L. Xiong, K. W. Post, S. S. Sunku, B.-Y. Jiang, J. Hone, C. R. Dean, M. M. Fogler, D. N. Basov, Fundamental limits to graphene plasmonics. *Nature* **557**, 530–533 (2018).

52. A. J. Giles, S. Dai, I. Vurgaftman, T. Hoffman, S. Liu, L. Lindsay, C. T. Ellis, N. Assefa, I. Chatzakis, T. L. Reinecke, J. G. Tischler, M. M. Fogler, J. H. Edgar, D. N. Basov, J. D. Caldwell, Ultralow-loss polaritons in isotopically pure boron nitride. *Nat. Mater.* **17**, 134–139 (2018).

53. N. Li, X. Guo, X. Yang, R. Qi, T. Qiao, Y. Li, R. Shi, Y. Li, K. Liu, Z. Xu, L. Liu, F. J. García de Abajo, Q. Dai, E.-G. Wang, P. Gao, Direct observation of highly confined phonon polaritons in suspended monolayer hexagonal boron nitride. *Nat. Mater.* **20**, 43–48 (2021).

54. Y. Li, A. Chernikov, X. Zhang, A. Rigosi, H. M. Hill, A. M. van der Zande, D. A. Chenet, E.-M. Shih, J. Hone, T. F. Heinz, Measurement of the optical dielectric function of monolayer transition-metal dichalcogenides: MoS$_2$, MoSe$_2$, WS$_2$, and WSe$_2$. *Phys. Rev. B* **90**, 205422 (2014).

55. I. Epstein, B. Terrés, A. J. Chaves, V.-V. Pusapati, D. A. Rhodes, B. Frank, V. Zimmermann, Y. Qin, K. Watanabe, T. Taniguchi, H. Giessen, S. Tongay, J. C. Hone, N. M. R. Peres, F. H. L. Koppens, Near-unity light absorption in a monolayer WS$_2$ Van der Waals heterostructure cavity. *Nano Lett.* **20**, 3545–3552 (2020).

56. G. M. Vanacore, I. Madan, G. Berruto, K. Wang, E. Pomarico, R. J. Lamb, D. McGrouther, I. Kaminer, B. Barwick, F. J. García de Abajo, F. Carbone, Attosecond coherent control of freeelectron wave functions using semi-infinite light fields. *Nat. Commun.* **9**, 2694 (2018).

57. M. A. M. de Aguiar, Exact Green's function for the step and square-barrier potentials. *Phys. Rev. A* **48**, 2567–2573 (1993).

58. K. F. Mak, M. Y. Sfeir, Y. Wu, C. H. Lui, J. A. Misewich, T. F. Heinz, Measurement of the optical conductivity of graphene. *Phys. Rev. Lett.* **101**, 196405 (2008).

59. R. R. Nair, P. Blake, A. N. Grigorenko, K. S. Novoselov, T. J. Booth, T. Stauber, N. M. R. Peres, A. K. Geim, Fine structure constant defines visual transparency of graphene. *Science* **320**, 1308 (2008).

60. M. Rocca, Low-energy EELS investigation of surface electronic excitations on metals. *Surf. Sci. Rep.* **22**, 1–71 (1995).

61. J. B. Pendry, *Low energy electron diffraction* (Academic Press, 1974).

62. J. B. Pendry, in *Determination of Surface Structure by LEED*, P. M. Marcus and F. Jona, Eds. (Plenum Press, 1984).

63. H. Claus, A. Büssenschütt, M. Henzler, Low energy electron diffraction with energy resolution. *Rev. Sci. Instrum.* **63**, 2195–2199 (1992).

64. T. Nagao, T. Hildebrandt, M. Henzler, S. Hasegawa, Dispersion and damping of a two-dimensional plasmon in a metallic surface-state band. *Phys. Rev. Lett.* **86**, 5747–5750 (2001).

65. T. Nagao, S. Yaginuma, T. Inaoka, T. Sakurai, Onedimensional plasmon in an atomic-scale metal wire. *Phys. Rev. Lett.* **97**, 116802 (2006).

66. M. Gulde, S. Schweda, G. Storeck, M. Maiti, H. K. Yu, A. M. Wodtke, S. Schäfer, C. Ropers, Ultrafast low-energy electron diffraction in transmission resolves polymer/graphene superstructure dynamics. *Science* **345**, 200–204 (2014).

67. S. Vogelgesang, G. Storeck, J. G. Horstmann, T. Diekmann, M. Sivis, S. Schramm, K. Rossnagel, S. Schäfer, C. Ropers, Phase ordering of charge density waves traced by ultrafast lowenergy electron diffraction. *Nat. Phys.* **14**, 184–190 (2018).

68. A. Weingartshofer, J. K. Holmes, J. Sabbagh, S. L. Chin, Electron scattering in intense laser fields. *J. Phys. B* **16**, 1805–1817 (1983).

69. P. Francken, C. J. Joachain, Theoretical study of electron-atom collisions in intense laser fields. *J. Opt. Soc. Am. B* **7**, 554–563 (1990).

70. V. Di Giulio, E. Arqué López, F. J. García de Abajo, Atomic Floquet physics revealed by free electrons. *Phys. Rev. Res.* **4**, 013241 (2022).

71. E. N. Economou, *Green's Functions in Quantum Physics* (Springer, 2006).

72. A. Messiah, *Quantum Mechanics* (North-Holland, 1966).

73. J. J. Sakurai, *Modern Quantum Mechanics* (Addison-Wesley, 1994).

74. D. M. Wolkow, Über eine Klasse von Lösungen der Diracschen Gleichung. *Z. Phys.* **94**, 250–260 (1935).

75. M. A. Van Hove, W. H. Weinberg, C.-M. Chan, *Low energy electron diffraction* (Springer-Verlag, 1986).

76. A. L. Ankudinov, S. I. Zabinsky, J. J. Rehr, Single configuration Dirac-Fock atom code. *Comput. Phys. Commun.* **98**, 359–364 (1996).

77. F. Salvat, R. Mayol, Accurate numerical solution of the Schrödinger and Dirac wave equations for central fields. *Comput. Phys. Commun.* **62**, 65–79 (1991).

78. F. J. García de Abajo, M. A. Van Hove, C. S. Fadley, Multiple scattering of electrons in solids and molecules: A cluster-model approach. *Phys. Rev. B* **63**, 075404 (2001).

79. K. Kambe, Theory of low-energy electron diffraction. *Z. Naturforsch. A* **22**, 322–330 (1967).